ACS APPLIED ENERGY MATERIALS

www.acsaem.org Article

# High-Performance Titanium Oxynitride Thin Films for Electrocatalytic Water Oxidation

Nikhil Reddy Mucha, Jacob Som, Jonghyun Choi, Surabhi Shaji, Ram K. Gupta, Harry M. Meyer, Corson L. Cramer, Amy M. Elliott, and Dhananjay Kumar*

Cite This: *ACS Appl. Energy Mater.* 2020, 3, 8366−8374 Read Online

ACCESS | Metrics & More | Article Recommendations

**ABSTRACT:** $TiN_xO_y$ (TiNO) thin films with superior electrochemical properties have been synthesized in situ using a pulsed laser deposition method and a varied oxygen partial pressure from 5 to 25 mTorr. The electrochemical overpotential of these TiNO films for water oxidation was found to be as low as 290 mV at 10 mA/cm$^2$, which is among the lowest overpotential values reported. The Tafel slopes, indicative of a rate of increase of electrode potential with respect to current, for these films are determined to be in the range of 85−57 mV/decade. These results further demonstrate the superiority of TiNO thin film as electrocatalyst for water oxidation to generate fossil-free fuels. The improvement in the electrocatalytic behavior of the semiconducting TiNO thin films is explained based on an adjustment in the valence band maximum edge and an enhancement in the number of electrochemically active sites. Both effects are realized by the substitution of N by O, forming a TiNO lattice that is isostructural with the rock-salt TiN lattice. These findings appear to assume significant importance in light of water electrolysis to produce fuels for the development of environmentally friendly power sources.

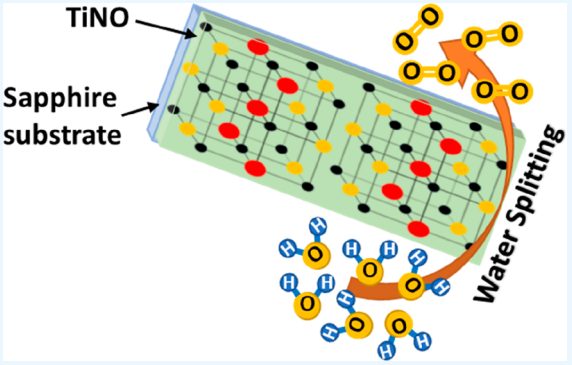


**KEYWORDS:** *oxynitrides, oxygen evolution reaction, electrocatalysis, electrochemical overpotential, water splitting, thin films, pulsed laser deposition*



## 1. INTRODUCTION

The research efforts toward developing easy-to-synthesize high conductivity anode electrocatalysts that are relatively inexpensive, stable, and active at low overpotentials during water splitting are challenging. The requirements for these developments are stringent and have often hindered the practical use of the precious metals such as Pt, Pd, Ru, Ir, etc. and oxides such as $RuO_2$, $IrO_2$ in the electrochemical systems. A large difference in the electronegativity values between titanium (Ti) and oxygen (O) as well as nitrogen (N) enables Ti to react easily with oxygen and nitrogen to form titanium dioxide ($TiO_2$) and titanium nitride (TiN). The simplicity of the synthesis and the embodiment of myriads of unique properties in TiN and $TiO_2$ place these two compounds among the most widely studied and used materials. After the work of Honda and Fujishima, $TiO_2$ has become a paradigm material in surface science and catalysis.[1−7] TiN exhibits an unusual combination of covalent, metallic, and ionic properties: ultrahardness (close to that of the diamond), high thermal conductivity, high electrical conductivity (higher than that of Ti), and even low- temperature superconductivity.[8−16] Several Ti-based oxynitrides ($TiN_xO_y$, abbreviated as TiNO) compounds, intermediate between metallic TiN and insulating $TiO_2$, have gained enormous scientific and engineering attention recently due to progressive and favorable change in their properties, opening the doors for many applications.[2,3,9,17−22] Oxynitride stabilities in air and moisture are greater than those of the pure nitrides but have smaller bandgap than those of comparable oxides.[20,22−29] There is no isostructural phase between TiN and $TiO_2$. However, TiN is isostructural with rock-salt $TiN_{0.5}O_{0.5}$ (obtained with 50% substitution of N by O in TiN).[19,30,31] The rock-salt structures of TiN and $TiN_{0.5}O_{0.5}$ are shown in Figure 1. Due to a random substitution of N by O and a concomitant change in the valence state of Ti, and consequently ionic radii, the lattice parameters (a, b and, c) along the x-, y-, and *z*-axis do not remain same. Accordingly, the three orthogonal angles ($\alpha$, $\beta$, and $\gamma$) would also deviate from 90°. Thus, the oxidation of TiN is expected to shift to monoclinic crystal symmetry from cubic.

**Received:** April 29, 2020
**Accepted:** August 4, 2020
**Published:** August 4, 2020

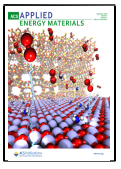




https://dx.doi.org/10.1021/acsaem.0c00988
*ACS Appl. Energy Mater.* 2020, 3, 8366−8374

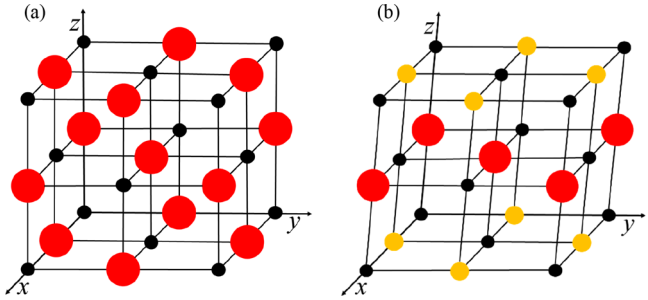


**Figure 1.** Unit cell crystal structures of (a) TiN and (b) $TiN_{0.5}O_{0.5}$: $Ti^{3+}$, black dot = 0.081 nm; $N^{3-}$, red dot = 0.132 nm; $O^{2-}$, yellow dot = 0.100 nm.

However, the base rock-salt type structure remains intact. Hence, it is favorable to oxidize TiN to TiNO as the incorporated O atoms are already in their most stable structure, namely, rock-salt. Moreover, in this way, the main drawback of an extra-electron transfer during N-incorporation in $TiO_2$ is overcome.[9,30−32]

The present study has focused on the synthesis of $TiN_xO_y$ thin films with varying $x$ and $y$ and the study of their performance in water splitting for oxygen evolution. The overpotentials for oxygen evolution reaction (OER; $4OH^- = O_2 + 2H_2O + 4e^-$)[33] realized for these films are in the range of 320 to 290 mV (at 10 mA/cm$^2$) which are among the lowest values reported for metal alloys, oxynitrides, and oxide systems, designed using extrinsic as well as intrinsic approaches.[3,17,27,34] The materials design via the extrinsic approach is generally based on increasing the loading capacity of the electrocatalysts via defect engineering and/or surface modification, while the intrinsic approach is based on exploring novel materials with an enhanced electroactivity.[35−37] The improvement in the electrocatalytic behavior of TiNO thin films is explained based on the enhanced number of electrochemically active sites realized by the substitution of anionic N sites by O and a favorable alignment of valence band with respect to the redox potential of electrolyte medium.[19,27] These findings are of significant importance in light of water electrolysis to produce fossil-free fuels for the development of environmentally friendly power sources.[35,38] Although there are some reports on the electrocatalytic activity of TiNO system, the majority of the reports are focused on the TiNO system in the polycrystalline bulk form.[3,39−42] The significance of TiNO thin film research arises from better possibilities in precisely controlling the orientation, crystallinity, composition, grain size, and grain distribution, which are well-known to critically affect the film's properties.[9,18,19,43−45] The TiNO material system in thin film form has also a strong potential for integration with technologically important substrates such as silicon and sapphire due to the small mismatch in lattice constants and thermal expansion coefficients.[46,47]

## 2. EXPERIMENTAL SECTION

TiNO films were deposited on single crystal c-plane sapphire (0001 orientation) substrates using a pulsed laser deposition (PLD) method. A high purity (99.99%) titanium nitride composite target was used to deposit TiNO films by controlling the oxygen pressure, substrate temperature, laser energy density, laser repetition rate, etc. An excimer laser (Coherent Complex Pro) with krypton fluoride (KrF) radiation (wavelength 248 nm, pulse duration 30 ns) was used during the PLD experiments. The frequency of the laser beam was 10 Hz. A fixed number of laser pulses (shots) of 20 000 (deposition time = 2000 s) was used. Some other parameters specific to our PLD experiments include substrate temperatures of 400 °C, oxygen pressure in the range of 5−25 m Torr, and the laser energy density of 2 J/cm$^2$. The details of our PLD setup are described elsewhere.[9,10,48−50] The crystallographic studies and phase purity of TiNO films were carried out using Bruker D8 advanced X-ray diffractometer. X-ray photoelectron spectroscopy (XPS) was performed using a Thermo Scientific (Waltham, MA, USA) model k alpha XPS instrument. Survey spectra were acquired for qualitative and quantitative analyses. High-resolution core level spectra were acquired for detailed chemical state analysis. The surface morphology of TiNO films was studied using Hitachi SU8000 scanning electron microscopy (SEM).

The electrical resistance of TiNO films was measured using a Quantum Design Physical Property Measurement System. The electrical resistivity ($\rho$) was determined using a standard four-probe measurement which eliminates the contributions from the contact resistance The expression used in the calculation is $\rho = \left(\frac{V}{I}\right)\left(\frac{wt}{l}\right)$, where $V$ is the voltage developed across two intermediate voltage probes, $I$ is the current applied through the two extreme probes, $w$ is the width of the sample, $t$ is the thickness of the sample, and $l$ is the distance between the two voltage probes. Thin gold wires (~0.1 mm diameter) were attached to four circular indium pads placed on the top surface of TiNO films. In this method, no conductive layer is needed from the bottom side of the TiNO films. In the calculation of $\rho$, the exact dimensions ($l \times w$) of TiNO samples were used which were measured to be 6.09 mm × 5.16 mm, 5.99 mm × 6.08 mm, 6.12 mm × 5.86 mm, and 6.03 mm × 5.88 mm for samples deposited under 5 mTorr, 10 mTorr, 15 mTorr, and 25 mTorr of oxygen, respectively.

The electrochemical activities of TiNO samples were analyzed using linear sweep voltammetry (LSV), cyclic voltammetry, and electrochemical impedance spectroscopy. The electrochemical properties were studied using Versatat 4-500 electrochemical workstation (Princeton Applied Research, USA). A three-electrode system was used for all these measurements: a reference electrode (Hg/HgO), a counter electrode (platinum), and a working electrode (TiNO thin films). The electrolyte solution used was 1 M KOH. LSV and CV were performed at a rate of 5 and 50 mV/s, respectively. All EIS measurements were conducted in an applied 10 mV of AC amplitude with the frequency range of 0.05 Hz to 10 kHz. The solution temperature was maintained at 25 °C during all electrochemical measurements. In the electrochemical measurements, contact was made from the TiNO side using a metallic crocodile clip and the sample was dipped in the 1 M KOH solution carefully so that the clip did not touch the solution. The electrical resistivity of the TiNO films is in milliohm·cm (mΩ·cm) range which is significantly low compared to those of conventional semiconductors. Hence realizing the electrical contacts using metallic crocodile clips is believed not to adversely affect any electrochemical measurements. The area of the sample submerged in the solution was measured carefully to measure the electrochemical current density.

## 3. RESULTS AND DISCUSSION

The XRD diffraction patterns recorded from TiNO thin films grown on single-crystal sapphire substrates in an oxygen pressure of 5, 10, 15, and 25 mTorr are shown in Figure 2. The thickness of these films, measured using cross-sectional scanning electron microscopy and surface profilometry, was 265, 255, 250, and 240 nm, respectively. These thickness values are also in agreement with the film thickness values inferred from the etch rate and time it takes to reach the substrate surface while recording the depth profile in the XPS measurements. The appearance of only a set of parallel planes (111) at 36.7° and (222) at 77.4° suggests that all the films are highly textured. Both (111) and (222) peaks match the JCPDS data of TiNO rock-salt structure. The increase in the full width at half-maximum (fwhm) of (111) and (222) peaks with


https://dx.doi.org/10.1021/acsaem.0c00988
ACS Appl. Energy Mater. 2020, 3, 8366−8374

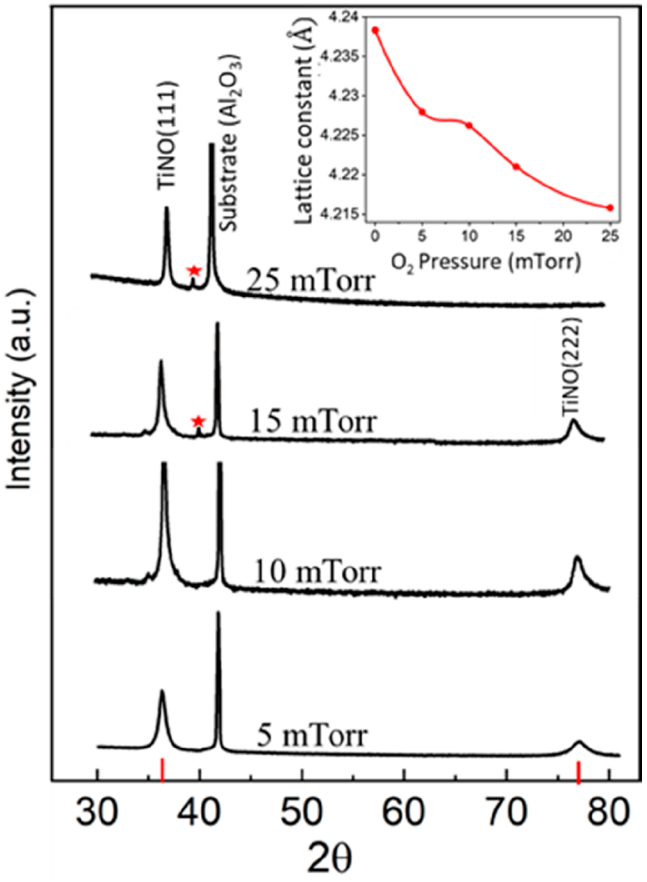


**Figure 2.** X-ray diffraction patterns of TiNO thin films grown at different oxygen pressures.

increasing oxygen pressure is attributed to a decrease in the average TiNO grain size at higher oxygen pressures.[9] A decrease in the film grain size at higher pressures is thought to be brought about by the enhanced vapor-phase collisions among the evaporated/ablated species. This, in turn, results in reduced adatom mobility on the substrate surface. The decrease in TiNO grain size and consequently the increase in the grain boundary density is manifested in the rise in electrical resistivity, as presented in the next section. A careful examination of the XRD patterns has shown that with an increase in oxygen pressure, the positions of both (111) and (222) peaks shift rightward with respect to pure TiN film peak positions, marked by two red lines on the *x*-axis. From the *d*-values of these peaks, lattice constants of the TiNO films were calculated as a function of oxygen pressures employed during growth, which is plotted in the inset of Figure 2.

As a reference, we have also plotted the lattice constant of a pure TiN film, which was grown in a vacuum of $1.6 \times 10^{-7}$ Torr with no intentional bleeding of oxygen to the growth chamber. The lattice constant of the pure TiN film (0.424 nm), determined using the XRD *d*-values, matches well to the theoretical lattice constant of TiN (0.426 nm) calculated using the ionic radii of $Ti^{3+}$ (0.081 nm) and $N^{3-}$ (0.132 nm) and rock-salt model of TiN lattice. The increase in the TiNO lattice constants progressively with an increase in the oxygen growth pressure (inset, Figure 2) is attributed to substitution of more N by O, which has smaller ionic radii (0.100 nm) with respect to that of N (0.132 nm). A minor peak corresponding to rutile $TiO_2$ has also been noticed at 41.2°, as marked by * in the diffraction patterns for TiNO films grown in oxygen pressures above 15 mTorr. The XPS results also confirm the trace presence of $TiO_2$ phase in TiNO film grown in higher oxygen pressures; however, the predominant phase remains TiNO in all the oxygen pressure ranges employed in the present study.[27,28] The SEM images of the surface morphology of TiNO films are displayed in Figure 3. All the images were

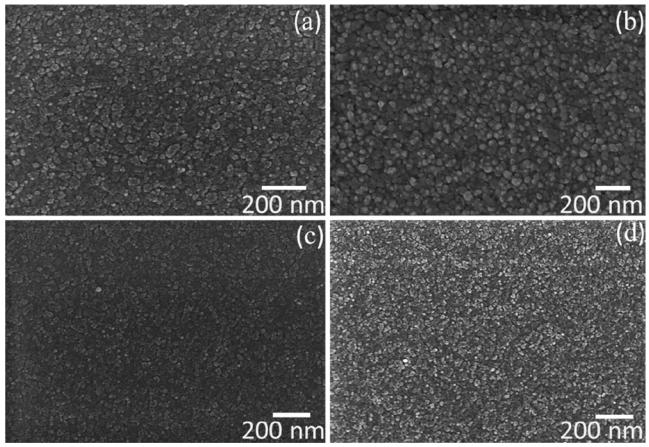


**Figure 3.** SEM images of TiNO films grown in oxygen pressures of (a) 5 mTorr, (b) 10 mTorr, (c) 15 mTorr, and (d) 25 mTorr.

recorded using the same magnification. It is clear from these images that all the films are smooth and are free from any particulates at this magnification. The TiNO grain size was found to be 100, 95, 80, and 65 nm in the TiNO films grown in 5, 10, 15, and 25 mTorr oxygen, respectively. The SEM grain size error was in the range of ±5 nm. The inverse dependence of the grain size on the oxygen pressure used during the film growth is attributed to higher gas phase inelastic collisions of the ablated species. The enhanced gas phase inelastic collisions result in lowering of the velocities of the forward moving ablated species that is manifested in the reduced surface mobility of the ablated species eventually arriving at the substrate surface and hence in the reduction in the net TiNO grain size.

The XPS spectra of $Ti_{2p}$, $O_{1s}$, and $N_{1s}$ recorded from the sputter clean TiNO samples are presented in Figure 4. The TiNO films were surface cleaned for 15 s by argon (Ar) ion etching to remove carbon, nitrogen, and oxygen adsorbed on the film surface from the ambient after TiNO depositions.[51] As seen in Figure 4a, the $Ti_{2p}$ spectrum consists of three distinct peaks. The Ti $2p_{3/2}$ peak (labeled P3) around 455 eV is associated with the Ti−N bonding in TiN. The peak, labeled P2, around 457 eV is associated with oxynitride (Ti−O−N). The peak (labeled P1) around 460 eV refers to the oxide component in $TiO_2$. The labeling of these peaks is based on the standard XPS peak parameters used for the evaluation of pure TiN and oxidized TiN samples.[9,51−54] TiN ($Ti_{2p3/2}$, 455.2 eV), Ti−N−O ($Ti_{2p3/2}$, 457.4 eV), $O^{2-}$ ($O_{1s}$, 530.1 eV), and $N^{3-}$ ($N_{1s}$, 397.2 eV). The intensity profile of these peaks indicates an overall decrease in P1 intensity coupled with an overall decrease in the intensity of P2 and P3 with increasing oxygen partial pressure used during the film deposition. The shift in the peak position from 530.78 to 530.48 eV for O 1s (Figure 4b) and from 396.58 to 396.48 eV for N 1s (Figure 3c) with an increase in oxygen pressure from 5 to 25 mTorr also lends credence to the increased level of oxidation of TiNO


https://dx.doi.org/10.1021/acsaem.0c00988
ACS Appl. Energy Mater. 2020, 3, 8366−8374

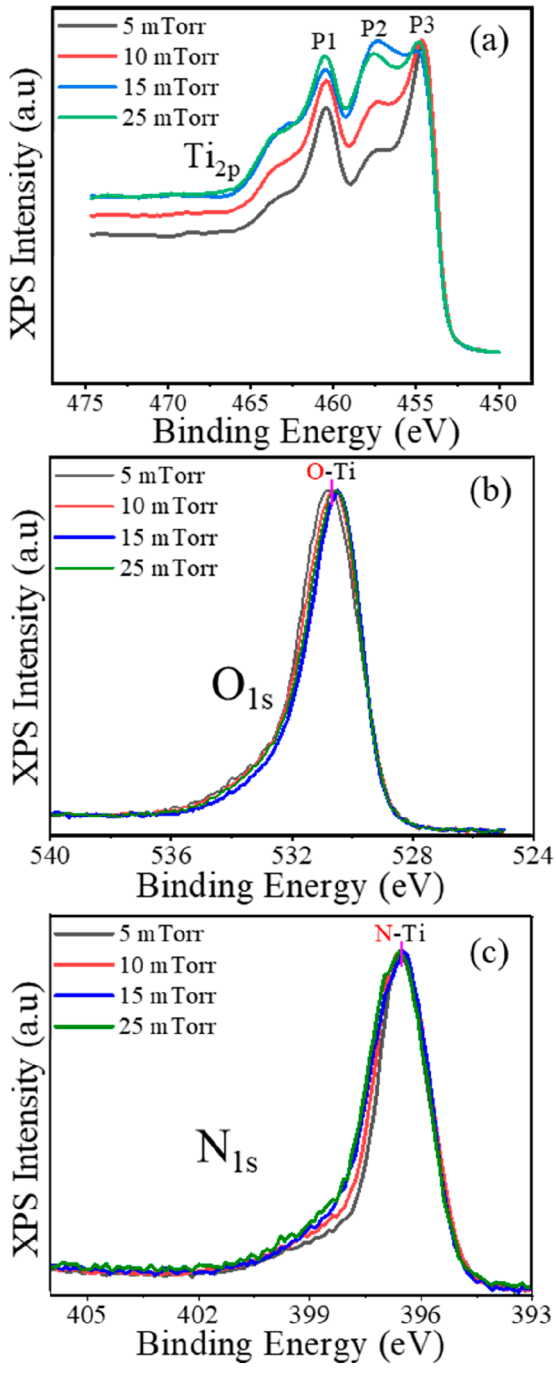


**Figure 4.** XPS spectra of (a) Ti 2p, (b) O 1s, and (c) N 1s recorded from sputtered clean TiNO films grown at different oxygen pressures.

films. The XPS compositions of the TiNO film deposited in 5, 10, 15, and 25 mTorr oxygen pressures were found to be $TiN_{0.57}O_{0.76}$, $TiN_{0.44}O_{0.99}$, $TiN_{0.37}O_{1.19}$, and $TiN_{0.29}O_{1.25}$ after 15 s of Ar-ion surface etch. The variation in the XPS elemental composition in the TiNO films due to a change in oxygen pressure is very informative in the calculation of substitutional point defects in TiNO films.

The variation of electrical resistivity of TiNO films, grown in different oxygen pressures keeping other deposition parameters constant, was studied as a function of temperature using a standard four-probe method and gold evaporated contacts. The normalized resistivity of TiNO thin film samples versus the temperature of measurements is shown in Figure 5. The

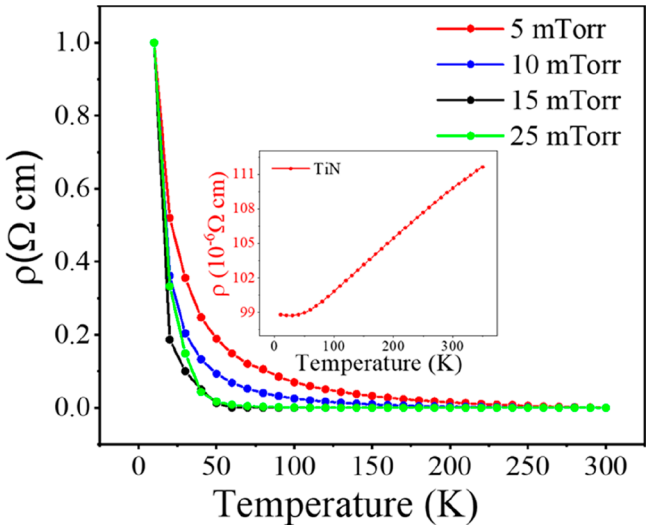


**Figure 5.** Normalized resistivity of TiNO thin films at various oxygen pressures with respect to temperature (inset) resistivity of pure TiN thin films.

normalization was carried out with respect to room temperature resistivity of the respective TiNO film to capture the variation of resistivity in one graph as their resistivity differed hugely due to differences in the oxygen growth pressures. The normalized resistivity values for all the films appear to be zero at 300 K in Figure 5. However, the actual values of 300 K resistivity are 6, 19, 36, and 69 mΩ·cm for TiNO films deposited in 5, 10, 15, and 25 mTorr oxygen pressure, respectively. The values of resistivity of these films at 200 K, 100 K, and 10 K are listed in Table 1. The decrease in

**Table 1. Resistivity Data of TiNO Films at Different Temperatures**

| oxygen pressure (mTorr) | 300 K (mΩ·cm) | 200 K (mΩ·cm) | 100 K (mΩ·cm) | 10 K (mΩ·cm) |
|---|---|---|---|---|
| 5 | 6.4 | 12.3 | 34.3 | 408.0 |
| 10 | 19.2 | 30.1 | 126.9 | 4481.0 |
| 15 | 36.3 | 80.1 | 189.0 | 2504500.0 |
| 25 | 69.3 | 313.9 | 5308.8 | 5383020.0 |

resistivity as temperature increases for all the films is indicative of their electrically semiconducting behavior. Shown, for comparison, is the resistivity plot for a TiN film grown under identical conditions but in high vacuum ($2 \times 10^{-7}$ Torr) with no external gas. The metallic characteristic (increase in resistivity as temperature increases) of a pure TiN film grown in a high vacuum condition is well reported.[10]

The conversion of metallic TiN to semiconducting TiNO films via oxygen doping is explained using a simple band diagram shown in Figure 6. The diagram shows that when N atoms in TiN are substituted by O atoms, the top edge of the valence band (VB) moves progressively up with respect to the valence band maximum edge position in the pure $TiO_2$. The position of the conduction band (CB) minimum due to Ti(3d) remains unaffected in the process of alteration taking place at the anion sites. The upward shift of the VB maximum in the oxynitride system with respect to the VB position in pure $TiO_2$ can be understood by considering the fact that the VB in the oxynitride is the hybrid of O(2p) and N(2p) orbitals. This bandgap engineering can also be looked at in an alternative


https://dx.doi.org/10.1021/acsaem.0c00988
ACS Appl. Energy Mater. 2020, 3, 8366−8374

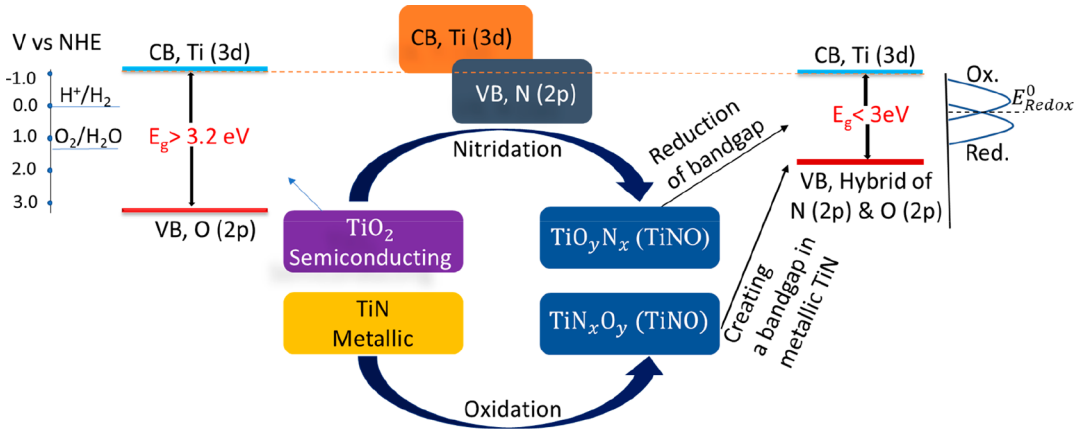


**Figure 6.** Band diagram showing a downward movement of VB via nitridation of $TiO_2$ and opening of a bandgap between overlapping valence and conduction band in a metallic TiN via oxidation of TiN.

manner.[19,55,56] The metallic characteristics of pure TiN are well explained due to an overlapping N(2p) VB and Ti(3d) CB, as represented in the central upper part of Figure 6. A substitution of N by O can lead to creating a gap between VB and CB that keeps increasing continually until the TiN phase is transformed fully to an insulating $TiO_2$ phase with a bandgap of more than 3.0 eV; also shown in the band diagram are the water oxidation and reduction potential ($V$) with respect to a normal hydrogen electrode (NHE). As illustrated in the right part of Figure 6, if the redox potential of an electrolyte is aligned well to either VB or CB, the water oxidation or reduction kinetics will be fast.[29,57,58]

The electrochemical performance of TiNO samples as efficient OER electrocatalyst has been investigated using linear sweep voltammetry (LSV) in 1 M KOH. The results obtained are shown in Figure 7a, where the current density is plotted as a function of sweeping potential for four samples that were made in oxygen pressures of 5 mTorr to 25 mTorr. Applying the standard 10 mA/cm$^2$ current density criterion, the overpotential of TiNO thin films deposited in 5, 10, 15, and 25 mTorr oxygen pressure are found to be 340, 320, 310, and 290 mV, respectively. The current density of 10 mA/cm$^2$ criterion is universally accepted because a device with 10% solar-to-hydrogen conversion efficiency produces this current density under 1-sun illumination.[34] A comparison of the overpotential values realized in the TiNO films with the reported values of OER overpotential in the recent work places the TiNO system among the well-established water oxidation catalysts in alkaline media. A few other examples are metal alloys, nitrides, and oxides such as FeCoNi (291 mV),[17] $Co_2N$ (413 mV), $Ni_3N$ (388 mV), FeCo (371 mV),[17] CoNi (366 mV), FeNi (350 mV),[17] Ir−C, $RuO_2$, and $IrO_2$,[17] NiFe-LDH single-layer nanosheets (302 mV),[59] monolayer NiV-LDH (318 mV),[60] $NiCo_2O_4$ ultrathin nanosheets (320 mV),[61] CoMnP nanoparticles (330 mV),[62] $Co_3O_4/NiCo_2O_4$ double-shelled nanocages (340 mV),[63] single crystal $Co_3O_4$@CoO (430 mV),[64] O-NiCoFe-LDH (420 mV),[65] and Ni−Co mixed oxide cages (380 mV).[66]

The kinetics of the OER of these films have been analyzed using Tafel slopes. The Tafel slopes are shown in Figure 7b that is obtained by plotting potential versus the log of the current density. The Tafel slopes are calculated to be 85, 74, 70, and 57 mV/decade for the TiNO films grown in 5, 10, 15, and 25 mTorr oxygen, respectively. These results also demonstrate the advantage of TiNO thin film catalysts. The Tafel slopes for TiNO films grown in 15 and 25 mTorr oxygen are lower than those in FeCoNi (63.8 mV/decade),[17] $IrO_2$ (87.3 mV), $RuO_2$ (136.1 mV/decade, and Pt/C (174.7 mV/decade), revealing its superior reaction kinetics.[17,27,67] The Nyquist plots obtained from the electrochemical impedance spectroscopy (EIS) measurements at 1.55 vs RHE are shown in Figure 7c. A simplified equivalent electrical circuit (EEC), shown in Figure 8, can be used to explain these EIS data. In the EEC, the electrochemical impedance spectra are represented as combinations of circuit elements such as resistors and capacitors. In this circuit, $R_1$ is the electrolyte resistance, $R_2$ is the charge transfer resistance at the interface (electrical double layer) between electrolyte and TiNO electrode, and $R_3$ is the resistance of the TiNO coating layer.[68−70] $C$ is the capacitance of the interfacial layer. The circuit shows that $R_1$ and $R_3$ are connected in series with $R_2$ and $C$. $R_2$ and $C$ are themselves connected in parallel as indicated by the dotted circle in Figure 8. The equivalent impedance/resistance of the circuit is given by

$$Z_{eq} = R_1 + \left(\frac{1}{\frac{1}{R_2} + \frac{1}{Z_C}}\right) + R_3 = R_1 + R_3 + \left(\frac{R_2}{1 + R_2 j\omega C}\right) \quad (1)$$

where $Z_C$ is the capacitance of the impedance, $j = \sqrt{-1}$, and $\omega$ is the angular frequency. The Nyquist plot arises from the electrical circuit contained in the dotted circle of Figure 7. The semicircle is characteristic of a single time constant, and its diameter ($Z'$ in Figure 6 c) represents the charge transfer resistance ($R_2$). The smaller is the diameter, the smaller is the charge transfer resistance and hence the faster is the reaction kinetics.[71−76] Thus, as seen in the Nyquist plots in Figure 7c, the TiNO film grown in 25 mTorr oxygen has the smallest diameter among all the films, indicating the least charge transfer resistance and hence the best electrochemical catalytic behavior.[72,74,77] It should be noted that the diameter of the Nyquist plot is not affected by the contact resistance of electrode materials since the diameter of the Nyquist plot is calculated from the difference of the high- and low-frequency $x$-axis data.

The improvement in the electrocatalytic behavior of TiNO thin films is explained based on proliferation in the number of active sites on the electrode surface by means of substitutional defects in the lattice.[4,78] As was seen in Figure 1, oxygen can


https://dx.doi.org/10.1021/acsaem.0c00988
ACS Appl. Energy Mater. 2020, 3, 8366−8374

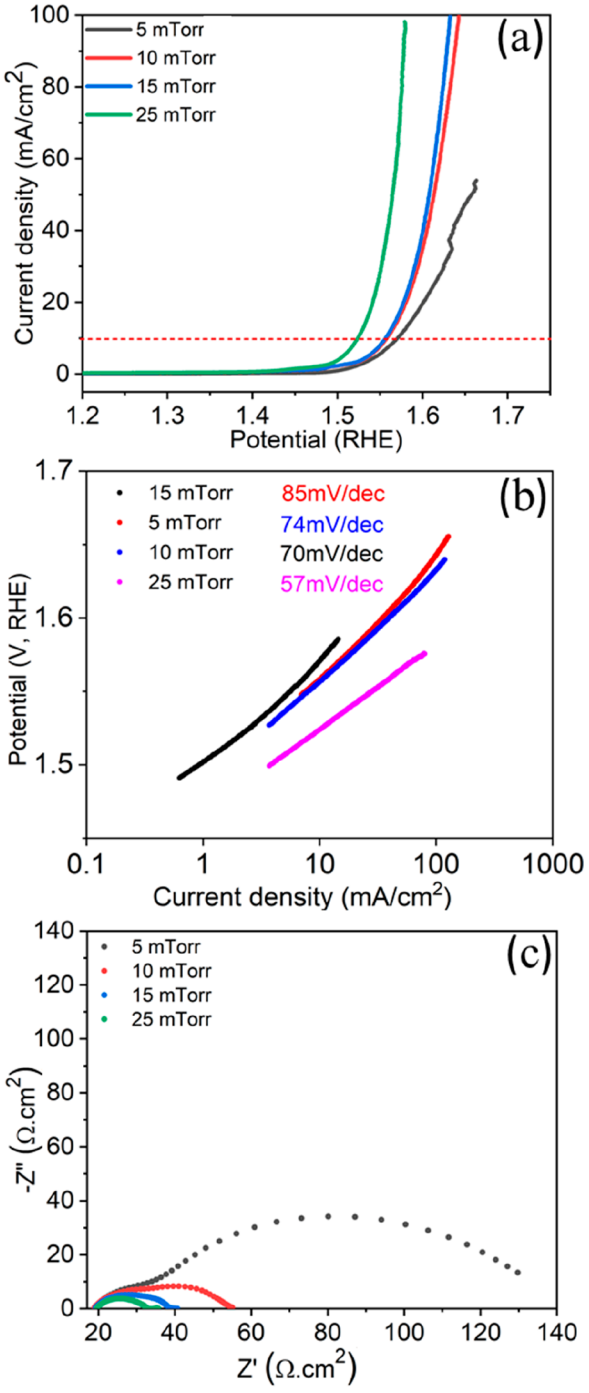


**Figure 7.** (a) Polarization curves, (b) Tafel plots, and (c) Nyquist plots for TiN thin films grown in 5, 10, 15, and 25 mTorr of oxygen pressure.

substitute nitrogen positions fully or partially in the TiN rock-salt lattice. Each substitutional site, a point defect in the lattice, serves as an active site for the OER reaction with an enhanced reaction rate. Using the XPS compositions described earlier ($TiN_{0.57}O_{0.76}$, $TiN_{0.44}O_{0.99}$, $TiN_{0.37}O_{1.19}$, and $TiN_{0.29}O_{1.25}$ films grown in 5, 10, 15, and 25 mTorr, respectively), the volume substitutional point defect densities in these films are calculated to be $2.2 \times 10^{22}/cm^3$, $2.9 \times 10^{22}/cm^3$, $3.4 \times 10^{22}/cm^3$, and $3.8 \times 10^{22}/cm^3$, respectively. The calculation of the volume substitutional point defect density is based on the maintenance of charge neutrality in the lattice and the

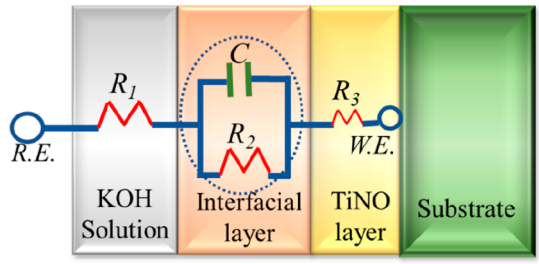


**Figure 8.** Schematic representation of an equivalent electrical circuit used to explain Nyquist plots. Note that the image is not to the scale; for example, the dimensions of the interfacial and TiNO layers are several orders of magnitude smaller than that of the substrate. R.E. is the reference electrode and W.E. is the working electrode.

protection of TiNO's rock-salt structure. To preserve these two conditions, oxygen in excess to the N and O stoichiometry additive value of unity leaves the lattice. The excess oxygen combines with Ti, which is also forced to leave the lattice to maintain the charge neutrality that comes in effect due to the substitution of trivalent N ions with bivalent oxygen ions. To illustrate this point, let us take the last sample with $TiN_{0.29}O_{1.25}$ composition. This composition could be alternatively written as $TiN_{0.29}O_{0.71+0.54}$. The first subscript number (0.71) on O stands for the fractional level of N substitution, while the second subscript number (0.54) on O stands for excess oxygen. Now, to maintain the charge neutrality in the lattice, 0.29 Ti ion per formula unit should leave the lattice, creating Ti cation vacancies in the lattice. Subsequently, 0.29 Ti and the excess 0.54 O are believed to combine to form an almost stoichiometric titanium oxide, $Ti_{0.29}O_{0.54}$ ($\equiv TiO_{1.9}$). It may be recalled that both XRD and XPS measurements have indeed shown the presence of $TiO_2$, especially for samples deposited in higher oxygen pressures. The surface densities of the substitution defects or equivalently the surface-active sites on the TiNO film surfaces, grown in 5, 10, 15, and 25 mTorr, are calculated by multiplying the volume density by the film's thickness assuming a uniform distribution of defects in the films' body. These values are found to be $5.8 \times 10^{17}/cm^2$, $7.4 \times 10^{17}/cm^2$, $8.5 \times 10^{17}/cm^2$, and $9.1 \times 10^{17}/cm^2$, respectively. Even if this calculation gives an approximate estimation of the surface density, a proportionality between volume defect density and surface defect density is well accepted. Thus, we have seen that TiNO film grown in 25 mTorr has the highest substitutional defects density among our samples, which results in the realization of the smallest OER overpotential and the fastest reaction kinetics.[4,78] Finally, the electrochemical stability of TiNO films has been tested by recording the current density as a function of time in the same electrolytic solution at an applied voltage of 1.55 V versus RHE. The results obtained are shown for all the four TiNO samples in Figure 9, which show that the current density decays almost negligibly for all the samples for 12 h. Though the time of this study is short, it demonstrates their stable electrochemical behavior which is critical for their practical application.[79]

## 4. CONCLUSIONS

In summary, a pulsed laser deposition method has been used to synthesize semiconducting thin film $TiO_xN_y$ compounds with varying $x$ and $y$ by simply changing the oxygen pressure during the film growth. The overpotential for oxygen evolution reaction realized for these films is in the range of 320−290 mV,


https://dx.doi.org/10.1021/acsaem.0c00988
ACS Appl. Energy Mater. 2020, 3, 8366−8374

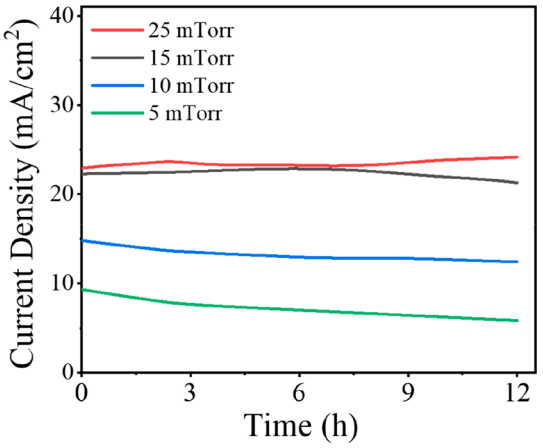


**Figure 9.** Time-dependent current density plots for TiNO films at 1.55 V vs RHE for 12 h.

which are among the lowest values reported for any oxynitride systems to date. The Tafel slopes for these films are determined to be in the range of 57−85 mv/decade. The improvement in the electrocatalytic behavior of TiNO thin films in terms of reduced OER overpotential and fast reaction kinetic is explained on the basis of an enhanced number of electrochemically active sites realized by the substitution of anionic N sites by O and a favorable alignment of valence band with respect to the redox potential of electrolyte medium. These findings appear to assume significant importance in light of water electrolysis to produce fossil-free fuels for the development of environmentally friendly power sources.

## AUTHOR INFORMATION


### Corresponding Author

**Dhananjay Kumar** − *Department of Mechanical Engineering, North Carolina Agricultural and Technical State University, Greensboro, North Carolina 27411, United States;* orcid.org/0000-0001-5131-5131; Phone: 336-285-3227; Email: dkumar@ncat.edu

### Authors

**Nikhil Reddy Mucha** − *Department of Mechanical Engineering, North Carolina Agricultural and Technical State University, Greensboro, North Carolina 27411, United States*

**Jacob Som** − *Department of Mechanical Engineering, North Carolina Agricultural and Technical State University, Greensboro, North Carolina 27411, United States*

**Jonghyun Choi** − *Department of Chemistry, Pittsburg State University, Pittsburg, Kansas 66762, United States*

**Surabhi Shaji** − *Department of Mechanical Engineering, North Carolina Agricultural and Technical State University, Greensboro, North Carolina 27411, United States*

**Ram K. Gupta** − *Department of Chemistry, Pittsburg State University, Pittsburg, Kansas 66762, United States;* orcid.org/0000-0001-5355-3897

**Harry M. Meyer** − *Center for Nanophase Materials Sciences, Oak Ridge National Laboratory, Tennessee 37831, United States*

**Corson L. Cramer** − *Energy and Transportation Sciences Division, Oak Ridge National Laboratory, Tennessee 37831, United States*

**Amy M. Elliott** − *Energy and Transportation Sciences Division, Oak Ridge National Laboratory, Tennessee 37831, United States*

Complete contact information is available at: https://pubs.acs.org/10.1021/acsaem.0c00988


### Notes

The authors declare no competing financial interest.

## ACKNOWLEDGMENTS

D.K. acknowledges the financial support from the National Science Foundation (NSF) through the Nebraska Materials Research Science and Engineering Center (MRSEC) Grant DMR-1420645 and the University of North Carolina (UNC) system for the seed funding via Interinstitutional Planning Grant (IPG). Graduate students N.R.M., J.S., and S.S. were supported by Grant DMR-1420645.

## REFERENCES


(1) Fujishima, A.; Honda, K. Electrochemical Photolysis of Water at a Semiconductor Electrode. *Nature* **1972**, *238*, 37.

(2) Brancho, J. J.; Bartlett, B. M. Challenges in Co-Alloyed Titanium Oxynitrides, a Promising Class of Photochemically Active Materials. *Chem. Mater.* **2015**, *27* (21), 7207−7217.

(3) Gebauer, C.; Fischer, P.; Wassner, M.; Diemant, T.; Jusys, Z.; Hüsing, N.; Behm, R. J. Performance of titanium oxynitrides in the electrocatalytic oxygen evolution reaction. *Nano Energy* **2016**, *29*, 136−148.

(4) Kuraganti, V.; Jain, A.; Bar-Ziv, R.; Ramasubramaniam, A.; Bar-Sadan, M. Manganese doping of MoSe2 promotes active defect sites for hydrogen evolution. *ACS Appl. Mater. Interfaces* **2019**, *11* (28), 25155−25162.

(5) Sinhamahapatra, A.; Jeon, J.-P.; Yu, J.-S. A new approach to prepare highly active and stable black titania for visible light-assisted hydrogen production. *Energy Environ. Sci.* **2015**, *8* (12), 3539−3544.

(6) Yang, J. Y.; Bullock, R. M.; DuBois, M. R.; DuBois, D. L. Fast and efficient molecular electrocatalysts for H2 production: Using hydrogenase enzymes as guides. *MRS Bull.* **2011**, *36* (1), 39−47.

(7) Zou, X.; Zhang, Y. Noble metal-free hydrogen evolution catalysts for water splitting. *Chem. Soc. Rev.* **2015**, *44* (15), 5148−5180.

(8) Kumar, D.; Oh, S. H.; Pennycook, S. J.; Majumdar, A. K. Scaling exponent within the side-jump mechanism of Hall effect size-dependence in Ni nanocrystals. *Appl. Phys. Lett.* **2008**, *93* (13), 133105.

(9) Mucha, N. R.; Som, J.; Shaji, S.; Fialkova, S.; Apte, P. R.; Balasubramanian, B.; Shield, J. E.; Anderson, M.; Kumar, D. Electrical and optical properties of titanium oxynitride thin films. *J. Mater. Sci.* **2020**, *55* (12), 5123−5134.

(10) Roy, M.; Mucha, N. R.; Ponnam, R. G.; Jaipan, P.; Scott-Emuakpor, O.; Yarmolenko, S.; Majumdar, A. K.; Kumar, D. Quantum interference effects in titanium nitride films at low temperatures. *Thin Solid Films* **2019**, *681*, 1−5.

(11) Jaipan, P.; Nannuri, C.; Mucha, N. R.; Singh, M. P.; Xu, Z.; Moatti, A.; Narayan, J.; Fialkova, S.; Kotoka, R.; Yarmolenko, S.; Scott-Emuakpor, O.; Binek, C.; Kebede, A.; Kumar, D. Influence of Gold Catalyst on the Growth of Titanium Nitride Nanowires. *Mater. Focus* **2018**, *7* (5), 720−725.

(12) Narayan, J.; Biunno, N.; Singh, R.; Holland, O.; Auciello, O. Formation of thin superconducting films by the laser processing method. *Appl. Phys. Lett.* **1987**, *51* (22), 1845−1847.

(13) Rasic, D.; Sachan, R.; Chisholm, M. F.; Prater, J.; Narayan, J. Room Temperature Growth of Epitaxial Titanium Nitride Films by Pulsed Laser Deposition. *Cryst. Growth Des.* **2017**, *17* (12), 6634−6640.

(14) Faruque, M. K.; M-Darkwa, K.; Xu, Z.; Kumar, D. Fabrication, characterization, and mechanism of vertically aligned titanium nitride nanowires. *Appl. Surf. Sci.* **2012**, *260*, 36−41.

(15) Gbordzoe, S.; Kotoka, R.; Craven, E.; Kumar, D.; Wu, F.; Narayan, J. Effect of substrate temperature on the microstructural properties of titanium nitride nanowires grown by pulsed laser deposition. *J. Appl. Phys.* **2014**, *116* (6), 064310.
(16) Sarkar, K.; Jaipan, P.; Choi, J.; Haywood, T.; Tran, D.; Mucha, N. R.; Yarmolenko, S.; Scott-Emuakpor, O.; Sundaresan, M.; Gupta, R. K.; Kumar, D. Enhancement in corrosion resistance and vibration damping performance in titanium by titanium nitride coating. *SN Appl. Sci.* **2020**, *2*, 949.
(17) Di, J.; Zhu, H.; Xia, J.; Bao, J.; Zhang, P.; Yang, S.-Z.; Li, H.; Dai, S. High-performance electrolytic oxygen evolution with a seamless armor core−shell FeCoNi oxynitride. *Nanoscale* **2019**, *11* (15), 7239−7246.
(18) Jia, L.; Lu, H.; Ran, Y.; Zhao, S.; Liu, H.; Li, Y.; Jiang, Z.; Wang, Z. Structural and dielectric properties of ion beam deposited titanium oxynitride thin films. *J. Mater. Sci.* **2019**, *54* (2), 1452−1461.
(19) Maeda, K.; Domen, K. Oxynitride materials for solar water splitting. *MRS Bull.* **2011**, *36* (1), 25−31.
(20) Rawal, S. K.; Chawla, A. K.; Chawla, V.; Jayaganthan, R.; Chandra, R. Effect of ambient gas on structural and optical properties of titanium oxynitride films. *Appl. Surf. Sci.* **2010**, *256* (13), 4129−4135.
(21) Sowińska, M.; Brizzi, S.; Das, C.; Kärkkänen, I.; Schneidewind, J.; Naumann, F.; Gargouri, H.; Henkel, K.; Schmeißer, D. Analysis of nitrogen species in titanium oxynitride ALD films. *Appl. Surf. Sci.* **2016**, *381*, 42−47.
(22) Yoo, J. B.; Yoo, H. J.; Jung, H. J.; Kim, H. S.; Bang, S.; Choi, J.; Suh, H.; Lee, J.-H.; Kim, J.-G.; Hur, N. H. Titanium oxynitride microspheres with the rock-salt structure for use as visible-light photocatalysts. *J. Mater. Chem. A* **2016**, *4* (3), 869−876.
(23) Shi, X.; Xu, L.; Le, T. B.; Zhou, G.; Zheng, C.; Tsuru, K.; Ishikawa, K. Partial oxidation of TiN coating by hydrothermal treatment and ozone treatment to improve its osteoconductivity. *Mater. Sci. Eng., C* **2016**, *59*, 542−548.
(24) Shin, P.-K.; Mikolajick, T. Alkali- and hydrogen ion sensing properties of LPCVD silicon oxynitride thin films. *Thin Solid Films* **2003**, *426* (1), 232−237.
(25) Morikawa, T.; Asahi, R.; Ohwaki, T.; Aoki, K.; Taga, Y. Band-Gap Narrowing of Titanium Dioxide by Nitrogen Doping. *Jpn. J. Appl. Phys.* **2001**, *40* (6A), L561.
(26) Tompkins, H. G. The initial stages of the oxidation of titanium nitride. *J. Appl. Phys.* **1992**, *71* (2), 980−983.
(27) Wang, W.; Savadogo, O.; Ma, Z.-F. Preparation of new titanium oxy nitride based electro catalysts using an anhydrous sol-gel method for water electrolysis in acid medium. *Int. J. Hydrogen Energy* **2012**, *37* (9), 7405−7417.
(28) Wu, Z.; Dong, F.; Zhao, W.; Guo, S. Visible light induced electron transfer process over nitrogen doped TiO2 nanocrystals prepared by oxidation of titanium nitride. *J. Hazard. Mater.* **2008**, *157* (1), 57−63.
(29) Zhang, J. Z. Metal oxide nanomaterials for solar hydrogen generation from photoelectrochemical water splitting. *MRS Bull.* **2011**, *36* (1), 48−55.
(30) Graciani, J.; Hamad, S.; Sanz, J. F. Changing the physical and chemical properties of titanium oxynitrides TiN 1− x O x by changing the composition. *Phys. Rev. B: Condens. Matter Mater. Phys.* **2009**, *80* (18), 184112.
(31) McKenna, K. P. Structure, electronic properties, and oxygen incorporation/diffusion characteristics of the $\sum$ 5 TiN(310)[001] tilt grain boundary. *J. Appl. Phys.* **2018**, *123* (7), 075301.
(32) Haydous, F.; Döbeli, M.; Si, W.; Waag, F.; Li, F.; Pomjakushina, E.; Wokaun, A.; Gökce, B.; Pergolesi, D.; Lippert, T. Oxynitride Thin Films versus Particle-Based Photoanodes: A Comparative Study for Photoelectrochemical Solar Water Splitting. *ACS Applied Energy Materials* **2019**, *2* (1), 754−763.
(33) Chang, S. H.; Danilovic, N.; Chang, K.-C.; Subbaraman, R.; Paulikas, A. P.; Fong, D. D.; Highland, M. J.; Baldo, P. M.; Stamenkovic, V. R.; Freeland, J. W.; Eastman, J. A.; Markovic, N. M. Functional links between stability and reactivity of strontium ruthenate single crystals during oxygen evolution. *Nat. Commun.* **2014**, *5* (1), 4191.
(34) Seitz, L. C.; Dickens, C. F.; Nishio, K.; Hikita, Y.; Montoya, J.; Doyle, A.; Kirk, C.; Vojvodic, A.; Hwang, H. Y.; Norskov, J. K.; Jaramillo, T. F. A highly active and stable $IrO_x/SrIrO_3$ catalyst for the oxygen evolution reaction. *Science* **2016**, *353* (6303), 1011−1014.
(35) Seh, Z. W.; Kibsgaard, J.; Dickens, C. F.; Chorkendorff, I.; Nørskov, J. K.; Jaramillo, T. F. Combining theory and experiment in electrocatalysis: Insights into materials design. *Science* **2017**, *355* (6321), eaad4998.
(36) Benck, J. D.; Hellstern, T. R.; Kibsgaard, J.; Chakthranont, P.; Jaramillo, T. F. Catalyzing the Hydrogen Evolution Reaction (HER) with Molybdenum Sulfide Nanomaterials. *ACS Catal.* **2014**, *4* (11), 3957−3971.
(37) Benck, J. D.; Chen, Z.; Kuritzky, L. Y.; Forman, A. J.; Jaramillo, T. F. Amorphous Molybdenum Sulfide Catalysts for Electrochemical Hydrogen Production: Insights into the Origin of their Catalytic Activity. *ACS Catal.* **2012**, *2* (9), 1916−1923.
(38) Kortlever, R.; Shen, J.; Schouten, K. J. P.; Calle-Vallejo, F.; Koper, M. T. M. Catalysts and Reaction Pathways for the Electrochemical Reduction of Carbon Dioxide. *J. Phys. Chem. Lett.* **2015**, *6* (20), 4073−4082.
(39) Wen, Z.; Cui, S.; Pu, H.; Mao, S.; Yu, K.; Feng, X.; Chen, J. Metal Nitride/Graphene Nanohybrids: General Synthesis and Multifunctional Titanium Nitride/Graphene Electrocatalyst. *Adv. Mater.* **2011**, *23* (45), 5445−5450.
(40) Avasarala, B.; Haldar, P. Electrochemical oxidation behavior of titanium nitride based electrocatalysts under PEM fuel cell conditions. *Electrochim. Acta* **2010**, *55* (28), 9024−9034.
(41) Suhadolnik, L.; Lašič Jurković, D.; Likozar, B.; Bele, M.; Drev, S.; Čeh, M. Structured titanium oxynitride (TiOxNy) nanotube arrays for a continuous electrocatalytic phenol-degradation process: Synthesis, characterization, mechanisms and the chemical reaction microkinetics. *Appl. Catal., B* **2019**, *257*, 117894.
(42) Dutta, S.; Indra, A.; Feng, Y.; Han, H.; Song, T. Promoting electrocatalytic overall water splitting with nanohybrid of transition metal nitride-oxynitride. *Appl. Catal., B* **2019**, *241*, 521−527.
(43) Chen, X.; Lou, Y.-B.; Samia, A. C. S.; Burda, C.; Gole, J. L. Formation of Oxynitride as the Photocatalytic Enhancing Site in Nitrogen-Doped Titania Nanocatalysts: Comparison to a Commercial Nanopowder. *Adv. Funct. Mater.* **2005**, *15* (1), 41−49.
(44) Chisaka, M.; Ando, Y.; Yamamoto, Y.; Itagaki, N. A Carbon-Support-Free Titanium Oxynitride Catalyst for Proton Exchange Membrane Fuel Cell Cathodes. *Electrochim. Acta* **2016**, *214*, 165−172.
(45) Kim, S. Y.; Han, D. H.; Kim, J. N.; Lee, J. J. Titanium oxynitride films for a bipolar plate of polymer electrolyte membrane fuel cell prepared by inductively coupled plasma assisted reactive sputtering. *J. Power Sources* **2009**, *193* (2), 570−574.
(46) Punugupati, S.; Kumar, R.; Nori, S.; Hunte, F.; Narayan, J. Structural, magnetic and magnetotransport properties of bi-epitaxial La0.7Sr0.3MnO3 (110) thin films integrated on Si (001). *Acta Mater.* **2016**, *106*, 40−47.
(47) Kumar, D.; Chattopadhyay, S.; Gilmore, W. M.; Lee, C. B.; Sankar, J.; Kvit, A.; Sharma, A. K.; Narayan, J.; Pietambaram, S. V.; Singh, R. K. Structural and magnetoresistance properties of La2/3Ca1/3MnO3 thin films on buffered silicon substrates. *Appl. Phys. Lett.* **2001**, *78* (8), 1098−1100.
(48) Shaji, S.; Mucha, N. R.; Fialkova, S.; Kumar, D. Morphological data on soft ferromagnetic Fe90Ta10 thin films. *Data in Brief* **2019**, *27*, 104714.
(49) Shaji, S.; Mucha, N. R.; Majumdar, A.; Binek, C.; Kebede, A.; Kumar, D. Magnetic and electrical properties of Fe90Ta10 thin films. *J. Magn. Magn. Mater.* **2019**, *489*, 165446.
(50) Shaji, S.; Mucha, N. R.; Giri, P.; Binek, C.; Kumar, D. Magnetic and magnetocaloric properties of Fe2Ta thin films. *AIP Adv.* **2020**, *10* (2), 025222.


https://dx.doi.org/10.1021/acsaem.0c00988
ACS Appl. Energy Mater. 2020, 3, 8366−8374

(51) Kuznetsov, M. V.; Zhuravlev, J. F.; Zhilyaev, V. A.; Gubanov, V. A. XPS study of the nitrides, oxides and oxynitrides of titanium. *J. Electron Spectrosc. Relat. Phenom.* **1992**, *58* (1), 1−9.
(52) Jaeger, D.; Patscheider, J. Single crystalline oxygen-free titanium nitride by XPS. *Surf. Sci. Spectra* **2013**, *20* (1), 1−8.
(53) Kuznetsov, M. V.; Zhuravlev, J. F.; Gubanov, V. A. XPS analysis of adsorption of oxygen molecules on the surface of Ti and TiNx films in vacuum. *J. Electron Spectrosc. Relat. Phenom.* **1992**, *58* (3), 169−176.
(54) Milošv, I.; Strehblow, H. H.; Navinšek, B.; Metikoš-Huković, M. Electrochemical and thermal oxidation of TiN coatings studied by XPS. *Surf. Interface Anal.* **1995**, *23* (7−8), 529−539.
(55) Martin, D. J.; Reardon, P. J. T.; Moniz, S. J.; Tang, J. Visible light-driven pure water splitting by a nature-inspired organic semiconductor-based system. *J. Am. Chem. Soc.* **2014**, *136* (36), 12568−12571.
(56) Maeda, K.; Domen, K. Photocatalytic Water Splitting: Recent Progress and Future Challenges. *J. Phys. Chem. Lett.* **2010**, *1* (18), 2655−2661.
(57) Thorne, J. E.; Li, S.; Du, C.; Qin, G.; Wang, D. Energetics at the Surface of Photoelectrodes and Its Influence on the Photoelectrochemical Properties. *J. Phys. Chem. Lett.* **2015**, *6* (20), 4083−4088.
(58) Kudo, A. Z-scheme photocatalyst systems for water splitting under visible light irradiation. *MRS Bull.* **2011**, *36* (1), 32−38.
(59) Song, F.; Hu, X. Exfoliation of layered double hydroxides for enhanced oxygen evolution catalysis. *Nat. Commun.* **2014**, *5* (1), 4477.
(60) Fan, K.; Chen, H.; Ji, Y.; Huang, H.; Claesson, P. M.; Daniel, Q.; Philippe, B.; Rensmo, H.; Li, F.; Luo, Y.; Sun, L. Nickel−vanadium monolayer double hydroxide for efficient electrochemical water oxidation. *Nat. Commun.* **2016**, *7* (1), 11981.
(61) Bao, J.; Zhang, X.; Fan, B.; Zhang, J.; Zhou, M.; Yang, W.; Hu, X.; Wang, H.; Pan, B.; Xie, Y. Ultrathin spinel-structured nanosheets rich in oxygen deficiencies for enhanced electrocatalytic water oxidation. *Angew. Chem., Int. Ed.* **2015**, *54* (25), 7399−7404.
(62) Li, D.; Baydoun, H.; Verani, C. u. N.; Brock, S. L. Efficient water oxidation using CoMnP nanoparticles. *J. Am. Chem. Soc.* **2016**, *138* (12), 4006−4009.
(63) Hu, H.; Guan, B.; Xia, B.; Lou, X. W. Designed formation of Co3O4/NiCo2O4 double-shelled nanocages with enhanced pseudocapacitive and electrocatalytic properties. *J. Am. Chem. Soc.* **2015**, *137* (16), 5590−5595.
(64) Tung, C.-W.; Hsu, Y.-Y.; Shen, Y.-P.; Zheng, Y.; Chan, T.-S.; Sheu, H.-S.; Cheng, Y.-C.; Chen, H. M. Reversible adapting layer produces robust single-crystal electrocatalyst for oxygen evolution. *Nat. Commun.* **2015**, *6*, 8106.
(65) Qian, L.; Lu, Z.; Xu, T.; Wu, X.; Tian, Y.; Li, Y.; Huo, Z.; Sun, X.; Duan, X. Trinary layered double hydroxides as high-performance bifunctional materials for oxygen electrocatalysis. *Adv. Energy Mater.* **2015**, *5* (13), 1500245.
(66) Han, L.; Yu, X. Y.; Lou, X. W. Formation of prussian-blue-analog nanocages via a direct etching method and their conversion into Ni−Co-mixed oxide for enhanced oxygen evolution. *Adv. Mater.* **2016**, *28* (23), 4601−4605.
(67) Mavrokefalos, C. K.; Patzke, G. R. Water Oxidation Catalysts: The Quest for New Oxide-Based Materials. *Inorganics* **2019**, *7* (3), 29.
(68) Bard, A. J.; Faulkner, L. R. *Electrochemical Methods: Fundamentals and Applications*; Wiley, 2001; Vol. *2*, Issue 482, pp 580−632.
(69) Orazem, M. E.; Tribollet, B. *Electrochemical Impedance Spectroscopy*; John Wiley & Sons, 2017.
(70) Wilson, J.; Schwartz, D.; Adler, S. B. Nonlinear electrochemical impedance spectroscopy for solid oxide fuel cell cathode materials. *Electrochim. Acta* **2006**, *51* (8−9), 1389−1402.
(71) Akram, R.; Khan, M. D.; Zequine, C.; Zhao, C.; Gupta, R. K.; Akhtar, M.; Akhtar, J.; Malik, M. A.; Revaprasadu, N.; Bhatti, M. H. Cobalt sulfide nanoparticles: Synthesis, water splitting and supercapacitance studies. *Mater. Sci. Semicond. Process.* **2020**, *109*, 104925.
(72) Ayom, G. E.; Khan, M. D.; Ingsel, T.; Lin, W.; Gupta, R. K.; Zamisa, S. J.; Zyl, W. E.; Revaprasadu, N. Flexible Molecular Precursors for Selective Decomposition to Nickel Sulfide or Nickel Phosphide for Water Splitting and Supercapacitance. *Chem. - Eur. J.* **2020**, *26*, 2693−2704.
(73) Guragain, D.; Zequine, C.; Poudel, T.; Neupane, D.; Gupta, R.; Mishra, S. Facile Synthesis of Bio-Templated Tubular Co3O4 Microstructure and Its Electrochemical Performance in Aqueous Electrolytes. *J. Nanosci. Nanotechnol.* **2020**, *20* (5), 3182−3194.
(74) Zequine, C.; Bhoyate, S.; Wang, F.; Li, X.; Siam, K.; Kahol, P. K.; Gupta, R. K. Effect of solvent for tailoring the nanomorphology of multinary CuCo2S4 for overall water splitting and energy storage. *J. Alloys Compd.* **2019**, *784*, 1−7.
(75) Gupta, R. K.; Mensah-Darkwa, K.; Kumar, D. Corrosion Protective Conversion Coatings on Magnesium Disks Using a Hydrothermal Technique. *J. Mater. Sci. Technol.* **2014**, *30* (1), 47−53.
(76) Mitchell, E.; Gupta, R. K.; Mensah-Darkwa, K.; Kumar, D.; Ramasamy, K.; Gupta, B. K.; Kahol, P. Facile synthesis and morphogenesis of superparamagnetic iron oxide nanoparticles for high-performance supercapacitor applications. *New J. Chem.* **2014**, *38* (9), 4344−4350.
(77) Fernández-Ibáñez, P.; de las Nieves, F. J.; Malato, S. Titanium Dioxide/Electrolyte Solution Interface: Electron Transfer Phenomena. *J. Colloid Interface Sci.* **2000**, *227* (2), 510−516.
(78) Zhao, Y.; Balasubramanyam, S.; Sinha, R.; Lavrijsen, R.; Verheijen, M.; Bol, A.; Bieberle-Hütter, A. Physical and chemical defects in WO3 thin films and their impact on photoelectrochemical water splitting. *ACS Applied Energy Materials* **2018**, *1* (11), 5887−5895.
(79) Lian, J.; Zhang, F.; Lu, S.; Jiang, W.; Hu, Q.; Li, D.; Zhang, B. Amorphous Fe−Co−P−C Film on a Carbon Fiber Paper Support as an Efficient Electrocatalyst for the Oxygen Evolution Reaction. *ChemElectroChem* **2019**, *6* (15), 3976−3981.


https://dx.doi.org/10.1021/acsaem.0c00988
*ACS Appl. Energy Mater.* 2020, 3, 8366−8374